 doi:10.20944/preprints202010.0524.v1

*Article*

# Deformation of Bioinspired MXene Based Polymer Composites with Brick and Mortar Structures: Computational Analysis

**Shreyas Srivatsa [1]*, Pawel Packo [2], Leon Mishnaevsky Jr. [3] and Tadeusz Uhl [1,]*, Krzysztof Grabowski [1]**

[1] Academic Center for Materials and Nanotechnology, AGH University of Science and Technology, Krakow, Poland; sshreyas@agh.edu.pl, tuhl@agh.edu.pl, kgrabow@agh.edu.pl
[2] Department of Robotics and Mechatronics, AGH University of Science and Technology, Krakow, Poland; pawel.packo@agh.edu.pl
[3] Technical University of Denmark, Roskilde, Denmark; lemi@dtu.dk
* Correspondence: sshreyas@agh.edu.pl, tuhl@agh.edu.pl; Tel.: +48-730-610-199 (S.S.), Tel.: +48-602-398-564

**Abstract:** Deformation behavior of MXene based polymer composites with bioinspired brick and mortar structures is analyzed. MXene/Polymer nanocomposites are modeled at microscale using bioinspired configurations of nacre-mimetic brick-and-mortar assembly structure. MXenes (brick) with polymer matrix (mortar) are modeled using classical analytical methods and numerical methods based on Finite Elements (FE). The analytical methods provide less accurate estimation of elastic properties compared to numerical one. MXene nanocomposite models analyzed with FE method provide estimates of elastic constants in the same order of magnitude as literature reported experimental results with good consistency. Bioinspired design of MXene nanocomposites results in the effective Young's modulus of the nanocomposite increase by 25.1 % and the strength (maximum stress capacity within elastic limits) increase by 42.3 %. The brick and mortar structure of the nanocomposites leads to interlocking mechanism between MXene fillers in polymer matrix, resulting in effective load transfer, good strength, and damage resistance. This is demonstrated in this paper by numerical analysis of MXene nanocomposites subjected to quasi-static loads.

**Keywords:** MXenes; Biomimicry; Micromechanical models; Finite Element Method; Brick-and-mortar structures; Computational Analysis; Effective Interface Model;

## 1. Introduction

The discovery of nanomaterials in the last few decades led to applications of these nanomaterials in the fields of battery technology [1], sensors [2,3], wireless communication [4], composites with ceramic and polymer matrix for multifunctional materials [5–7] etc. Various nanomaterials like Carbon Nanotubes (CNTs), Graphene, Molybdenum di-sulfide, Boron Nitride etc. were used as fillers with polymer matrices to form nanocomposites with new desired functionalities. Recently, MXenes – two-dimensional (2D) materials discovered in 2011 [8] - have gained a lot of interest in various fields of applications due to their unique physical properties such as good conductivity, film-forming ability, good elasticity, etc. MXenes are inorganic compounds of metal carbides or nitrides. The MXene compound discovered in 2011 was Titanium Carbide ($Ti_3C_2T_x$, where surface termination $T_x$ can be -O, -OH or -F; physical properties used for the paper). The surface termination of MXenes which is naturally present due to chemical synthesis process results in hydrophilic behavior while the presence of metal atoms results in good conductivity [8]. The hydrophilic behavior exhibited by MXenes has an advantage over other nanomaterials such as unfunctionalized CNTs which tend to form agglomerates resulting in unpredictable behavior [8,9]. Moreover, hydrophilicity allows MXenes to be uniformly dispersed within a polymer matrix, therefore providing highly repeatable fabrication procedure. On the other hand, mechanical properties of monolayer MXenes are reported

 doi:10.20944/preprints202010.0524.v1



to be better than commercially available reduced-Graphene Oxides (r-GO) which are used extensively for applications with Graphene [10]. These advantages of MXenes provide unique opportunities to progress from the current state of the art in nanocomposites.

MXene monolayers (delaminated form or flakes) are most often used as fillers with polymer matrix materials resulting in MXene Nanocomposites (MXNC) [9],[11]. Though pure MXene films have good mechanical properties and conductivity [9], [12], these are not chemically stable for long time duration due to oxidation [13] making it brittle and unfit for use along with reduced conductivity. The same literature work also indicates the use of polymer material as matrix for MXene nanomaterials to provide a chemically stable film without oxidation. Varying MXene-to-polymer weight fraction and fabrication process result in a wide range of electrical and mechanical properties [9,11,14], creating space for tailoring a MXNC for specific application. This complex design process requires numerous and costly experimental procedures to find proper combination of process and material parameters for obtaining desired functionality of composites. The recently demonstrated brick-and-mortar (or layer-by-layer) assembly process of MXenes with controlled polymer intercalation provides a solution for controllable tailor-made fabrication process that can be modeled with analytical and numerical methods [15,16].

Pre-design of MXNC using analytical and numerical models plays a major role in overcoming the challenge posed by extensive physical testing of nanocomposites with different nanocomposite constituents. Models not only help in estimating the effective (overall) nanocomposite physical properties but also aid predicting behavior of the nanocomposite to various loading types and scenarios (mechanical, electrical, or electromagnetic etc.). Developing models for such nanocomposites involves complexity in geometry and material properties from nano to macro scale due to the size- and scale-effect phenomenon observed in composites, calling for multiscale modeling approaches. Several multiscale modeling strategies, as well as numerical techniques dedicated for nano-, micro-, meso- and macro-scale, and coupling procedures exist [17–20]. Despite a wide variety of existing numerical tools for predicting mechanical properties of materials in multiscale, their application to predicting behavior of MXenes is very limited. Among the approaches developed so far, works on nanoscale modeling and estimating mechanical properties of MXenes with molecular dynamic techniques can be mentioned [21,22]. Recently, few works on microscale modeling of MXene/Polymer nanocomposite has been reported and it uses a Finite Element Method for numerical mechanical analysis of such models [23], [24]. Therefore, noting the very limited number of works on modeling of MXene nanomaterials, we develop microscale mechanical models for bioinspired nacre-mimetic assembly MXNC.

In this paper, we consider the bioinspired brick-and-mortar structures of MXene/Polymer nanocomposites. The studies into tensile deformation of nacre at micro and macroscales [25] have led to nacre-mimetic pre-design of nanocomposites [26,27]. The brick-and-mortar assembly of the nacre provides topological and structural assembly advantages (interlocking mechanism) for the biocomposite to have greater strength and toughness than its main constituent [28]. We utilize these design benefits and develop pre-design configurations for MXene/Polymer nanocomposites. The paper provides the first instance of micromechanical modeling and analysis study incorporating the bioinspired nacre-mimetic assembly of MXene/Polymer nanocomposites.

Biomaterials in nature have inspired engineers for ages to develop composite materials for various applications [29]. Among these bioinspired materials and related pre-design, there have been efforts to mimic the bio-composites and develop man-made composites with enhanced strength, toughness, elasticity and damage resistance capabilities [30,31]. The biocomposites considered for pre-design in this paper is nacre, mother of pearls. Nacre has a strength and toughness higher than its main constituent material of calcium carbonate. Investigations of nacre over the years have led to micro and meso scale designs biomimicking the nacre-mimetic brick and mortar structure [32,33].

The structure of this paper is organized and discussed henceforth. First, geometric and material properties of MXenes are summarized based on the literature review outcome along with the experimental characterization tests carried out by the authors (provided in section 3.1). Then, approaches of modeling of a single MXene layer (flake) and MXene/Polymer nanocomposite based

on nacre-mimetic structure are discussed. MXNC films formed via brick-and-mortar (layer-by-layer) [26] assembly (same models can be applied to vacuum-assisted filtration [9,11], [34] process formed MXNCs but the stacking and layer-by-layer formation is not controlled) are the focus of these model developments. The consistent stack formation of MXene with polymer material provides the basis for deterministic model configurations considered later. Subsequently, analytical and numerical methods with potential applicability to modeling MXNC - like EIM [35], CLPT [13], [36] and FEA - are discussed and used. Finally, comparison between the reported experimental results and results obtained from all the MXNC models employed in this paper are given. This leads to discussions about the brick-and-mortar assembly during fabrication between MXene and polymer and their influence on the effective nanocomposite behavior. The paper concludes with the discussion of results.

For the purpose of modeling and properties estimation, volume fractions and weight fractions of MXenes and polymer will be used throughout this paper. Weight fraction to volume fraction conversion can be done based on the density of the filler and matrix, and the volumes depend on the models developed in this paper. The units used in the paper are mm, N, t/mm$^3$ unless otherwise stated.

## 2. Modeling and Methods

### *2.1. Mechanical properties of MXenes and polymers*

#### 2.1.1. MXenes

Geometrical properties of MXene monolayers have been studied extensively and the results [9], [11] of morphology and characterization of MXenes developed in the last few years with the synthesis process of in-situ HF formation with MILD method, indicate an average lateral dimension of MXene monolayers to be in the range of few microns (1-10 μm, without sonification) and the thickness to be in the range of few nanometers (1-10 nm) [37]. The lateral dimensions of 2 microns and thickness of 2 nm is used for all the MXene monolayer models in this paper.

The elastic properties of MXene monolayer are determined through experiments like nanoindentation using Atomic Force Microscopy [10] and various computational processes in literature on Molecular Dynamics [13], [21] and Density Functional Theory [38,39] have been used. The Density Functional Theory (DFT) was used in [38] to estimate Young's modulus and Poisson's ratio as 312 GPa and 0.2260 in one direction and 313 GPa and 0.2270 in the other lateral direction, respectively. The prediction from the DFT is well within the standard deviation bounds of the experimentally determined Young's modulus of MXene monolayer (330 ± 30 GPa) in [9]. It is also to be noted that the prediction from Molecular Dynamics (MD) gives an overestimation of the Young's modulus [13] to be 502 GPa. For this paper, the DFT study prediction is considered. The estimation provides Young's modulus values in the lateral directions of the MXene monolayer, so average values of Young's modulus and Poisson's ratio in the two lateral directions are taken and provided in Table 1.

**Table 1.** MXene physical properties [38]

| Mechanical Properties | Symbol (Unit) | Values |
|---|---|---|
| Young's Modulus in planar direction | E (GPa) | 312.5 |
| Poisson's ratio in the planar direction | μ | 0.2265 |
| In-plane shear modulus | G (GPa) | 141 |
| Density | ϱ (tmm-3) | ~3.2×10-9 |
| Maximum allowable Tensile stress | MPa | 17.3±1.6 ×103 |

Preprints (www.preprints.org) | NOT PEER-REVIEWED | Posted: 26 October 2020 doi:10.20944/preprints202010.0524.v1



2.1.2. Polymers

Two polymers are considered in the process of analysis in this paper, namely, epoxy-resin and Polyvinyl Alcohol (PVA). The material properties of PVA are - Young's modulus of 1 GPa, Poisson's ratio of 0.42, density of 1.19×10-9 tmm-3 and allowable maximum stress of 30MPa; material properties of epoxy-resin are - Young's modulus of 3.0741 GPa, Poisson's ratio of 0.29, density of 1.1×10-9 tmm-3 and allowable maximum stress of 49.9 MPa [9,26],[37,40,41].

*2.2. Analytical methods*

Once the properties of single-layer MXene model are defined, model for a MXNC is built by distributing several flakes along with polymer. The topology is based on deterministic configurations derived from MXNCs samples fabricated by brick-and-mortar (layer-by-layer) assembly (similar method can be used for vacuum-assisted filtration fabricated samples as well). The polymer and MXenes are modeled as a representative volume cube within which the MXene monolayers are orderly distributed for defining the volume fractions of each constituent in the composite used in the analytical model. The analytical methods of EIM and CLPT – used in this study - consider the interface between a MXene monolayer and polymer. A generic MXNC model with a set of MXene flakes with polymeric matrix is shown in Figure 1. The model assumes the interface layer to have the same shape as the filler.

There are two interfaces defined in this paper, namely, the filler-matrix-filler interface (in case of stack formed with MXenes and polymer) and filler-matrix (between MXene monolayer and polymer) interface. Both these interfaces are assumed to have the same elastic properties for EIM and CLPT method. The analytical models help in studying the effective MXNC elastic properties and compare it with the reported experimental results.

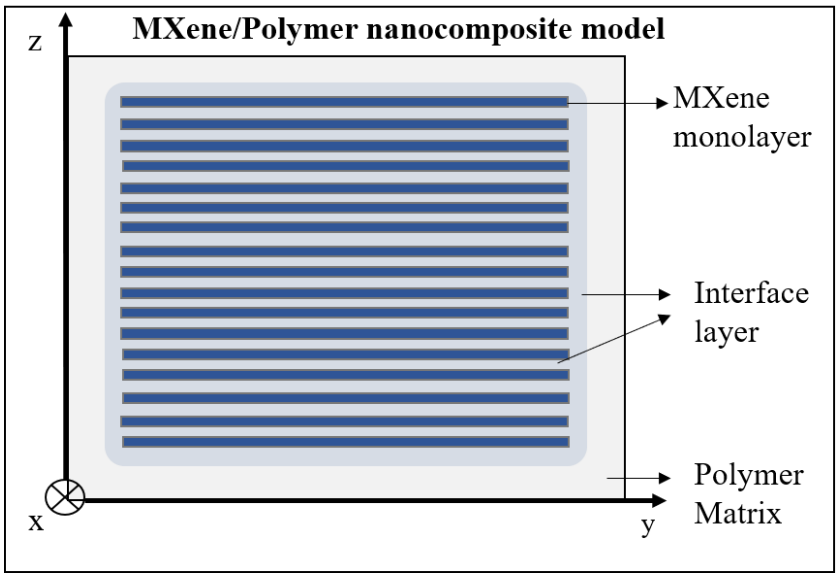


**Figure 1.** MXene/Polymer nanocomposite model representation at micro scale without MXene overlaps and coordinate axes of X, Y and Z which are orthogonal to each other

Effective Interface Model: The Effective Interface Model is a modified approach of the continuum mechanics-based Mori-Tanaka model [35]. The latter is based on analytical considerations of the Eshelby's inclusion principle [42,43]. The model considers the filler, matrix and interface material of the MXNC. In determining mechanical response of a MXNC, MXene monolayers are assumed to be distributed in an infinite space of polymer matrix material. In that setup, in EIM, the MXene flake is considered as the inclusion [44]. Based on the dimensions of MXenes considered in section 2.1.1, the MXene flake is approximated according to Eshelby's inclusion as a penny shaped

 doi:10.20944/preprints202010.0524.v1



inclusion (L=B>>h) for the purpose of forming the Eshelby's tensor which is basically a tensor based on geometric properties of the inclusion or filler (in this case: the MXene flake). Here the filler-matrix-filler interface and filler-matrix interface are assumed to have the same properties as discussed before. The drawback of the method is that a single filler material with interface is assumed in an infinite matrix space around it, thus the stacking and MXene assembly effect due to the fabrication process cannot be captured from this model. The equations for EIM formulation are provided in Appendix A.

Classical Laminate Plate Theory: Although a single MXene layer behaves membrane-like, the resulting bioinspired nacre-mimetic MXNCs display mechanical properties that may be effectively modelled via continuum-based approaches for plates. This is valid for a stacked sequence of MXene flakes embedded in a polymeric matrix, making such a composite setup very similar to a multilayered composite (shown in Figure 1). The MXNC is modeled using the CLPT model to estimate the effective elastic properties of the MXNC and incorporate the interface layers and provide estimations of their elastic properties. Here, the Kirchhoff's Plate theory – assuming the normal material line being infinitely rigid along its own length, normal material line of the plate remaining a straight line after deformation and normal material line being normal to the deformed plane of the plate – is considered for modeling of MXNCs [36]. The method considers a MXene flakes as thin plates (with small displacement and rotations and small strains) with polymer material between them. The assumptions for displacements and strains leading to equations are provided in Appendix B. The in-plane stiffness matrix of the formulation provided in Appendix B is considered for this paper as we only consider tensile loading of the MXNC film model.

### *2.3. Numerical methods*

Limitations of analytical modeling techniques related to shapes, thicknesses, distribution, interactions between the inclusions and other aspects, lead to application and developments of numerical methods for predicting mechanical responses of MXenes and bioinspired MXNCs. A common choice is the widely used and versatile finite element method. Among many tools and techniques available in Finite Elements, the so-called Multi-point Constraints (MPCs) can be effectively used for modeling MXenes with polymer material. In the proposed numerical model, MXene flakes and the polymer matrix are meshed independently, while the two sets of meshes do not need to be congruent (i.e. no common nodes are required). Next, the nodes of the MXene flakes are tied to the nearest nodes of the polymer matrix via MPCs. This allows linking of the field variables (displacements, temperatures, currents etc.) at nodes of MXene flakes with the field variable at the nodes of the polymer. For setting up the MPC equations, the interface is assumed to be perfectly bonded between the filler (MXene) and matrix (polymer). Figure 2 (a – c) illustrates configurations used for modeling MXNC. These topological distributions are based on the bioinspired nacre-mimetic brick-and-mortar assembly. Configuration 1 consists of a simple MXene/Polymer nanocomposite model while configuration 2 and 3 utilize nacre-mimetic nanocomposite assembly. The MXene/Polymer nanocomposites, modeled as RVEs [45,46] with a cube configuration at the micro scale, can later be used for hierarchical material framework for multi-scale analysis. The representative volume cube of 3.3 μm as the side length is considered.

Preprints (www.preprints.org) | NOT PEER-REVIEWED | Posted: 26 October 2020 doi:10.20944/preprints202010.0524.v1



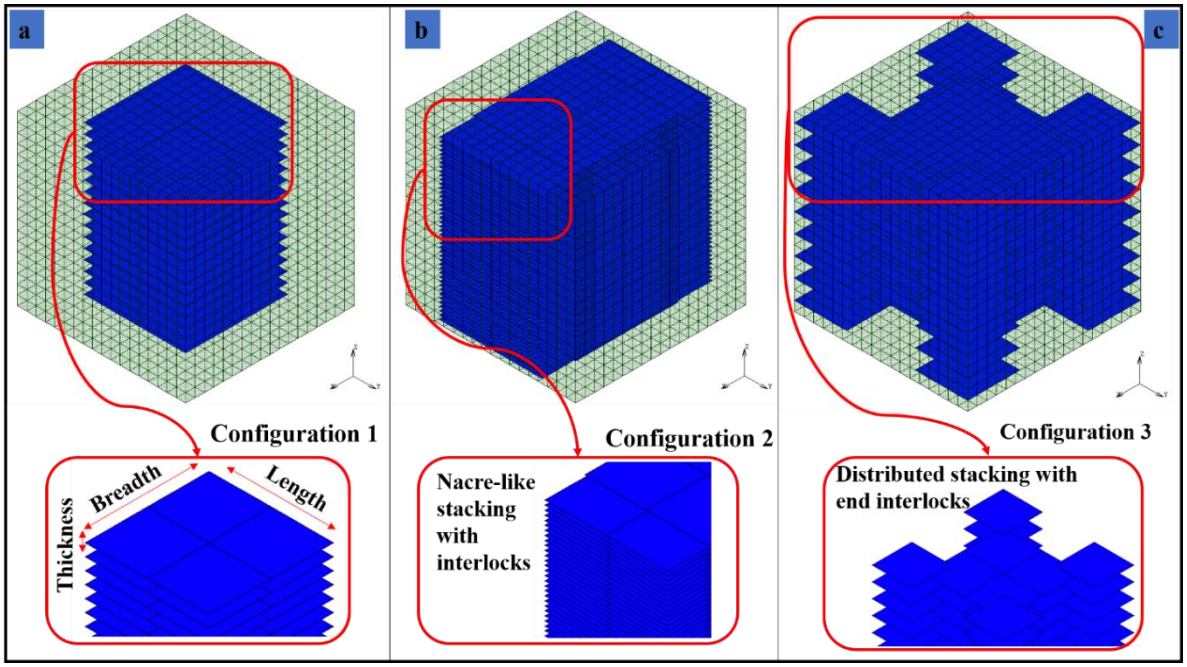


**Figure 2.** RVE configurations of MXene/Polymer nanocomposite. (a) Configuration 1, (b) Configuration 2, (c) Configuration 3

Element selections: A single MXene layer in the RVE is modeled using thick plate elements. Present models were implemented in MSC Marc software, therefore shape function details are provided in [47]. Material properties used for the model are given in section 2.1. Unlike the CLPT analytical model which has thin plate assumption, thick plate element in the numerical model uses the modified version of Mindlin-Reissner plate model [48] whose original version is also sometimes called in literature as the First-Order Shear Deformation Theory (FSDT) [49]. The FSDT theory assumes the normal material line, initially normal to the mid-plane of the plate, remains straight and unstretched after deformation, but not necessarily normal to the mid-plane of the plate. This leads to the finite rotations of the cross-section of the plate to be considered. The present modification [48] of the theory for thick plate element consists of formulation of parabolic distribution of transverse shear strains and satisfies the zero transverse shear stress requirements at the plate surfaces. The set of assumptions on strain of these thick plate elements is provided in Appendix C for further reference. The polymeric matrix is represented by eight-node three-dimensional brick elements with trilinear interpolation. These elements have three global displacements as degrees of freedom at each node along with eight-point Gaussian integration. Details on element's shape function formulation are given in Appendix C.

Numerical models of MXNCs are subjected to the test conditions similar to experimental works in literature [9] in order to estimate their mechanical properties via a virtual tensile test [32]. For a 1-D tensile test setup and uniform strain field, the upscaling procedure may be omitted, i.e. the results can be directly read from RVEs, provided that each RVE represents an infinitesimal representative element of the microstructure, following the Saint-Venant's principle. Therefore, RVEs built are initially loaded by a quasi-static uniaxial displacement boundary condition at one end and are fixed at the other end. Periodic boundary conditions along with the Hill-Mandel condition [46,50,51] are applied to obtain elastic properties of the MXNC from RVEs. This has been implemented in MSC Marc through in-house Fortran subroutines and quantitative results are provided in subsequent sections.

Preprints (www.preprints.org) | NOT PEER-REVIEWED | Posted: 26 October 2020 doi:10.20944/preprints202010.0524.v1



## 3. Results and discussions

### *3.1. Experimental characterization of MXene samples*

The MXene ($Ti_3C_2T_x$; supplied by Materials Research Centre, Ukraine) sample morphology and structure were investigated using TEM (Tecnai TF 20 X-TWIN) and SEM (Versa 3D scanning electronic microscope with field electron gun and ion) and lateral dimensions and single layer thicknesses were measured. Figure 3 (a) and (b) show the stack of pure MXenes flakes observed using HR-TEM. The thickness of this MXene sample was approximately 1-2 nm, confirming other literature studies (thickness of 1-10 nanometers and lateral dimensions being of the order of 1-10 microns). Figure 4 provides Energy Dispersion X-ray (EDX) spectroscopic data of MXene samples confirming the presence of Titanium Carbide with surface termination. Combining these and other geometrical features of MXenes (see e.g. [9]) provides data for subsequent construction and use of MXNC models developed in section 2.

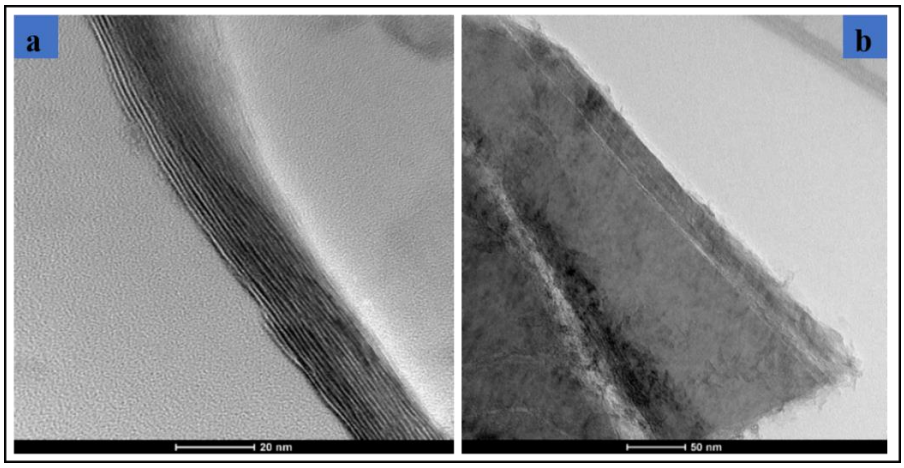


**Figure 3.** (a) & (b) HR-TEM images of stacks of pure MXene samples

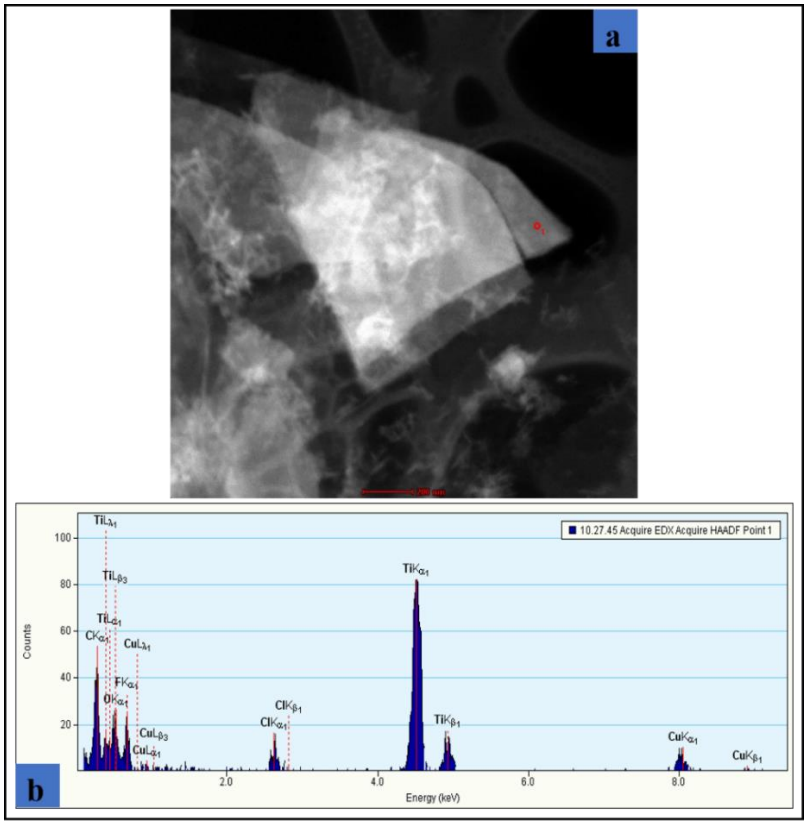

 doi:10.20944/preprints202010.0524.v1



**Figure 4.** (a) TEM image of MXene flakes (b) EDX analysis of the elemental composition

*3.2. Estimations of effective Young's modulus of MXNC*

The two analytical models are implemented for the various volume fractions of MXenes in polymer. The model parameters are shown in Table 2. Various deterministic configuration implemented for numerical models are marked (Table 2) for the same volume fractions. MXene/Epoxy-resin nanocomposite simulation results and quantitative comparison of results with reported experimental ones are shown in Table 3 and results for MXene/PVA nanocomposite are shown in Table 4.

Analytical models of EIM and CPLT are implemented based on their respective formulation in MATLAB code form. The models are tuned for the volume fractions of MXene in polymer. The total volume of these models is defined using a representative volume cube for purpose of providing volume constrains on the models developed. The number of MXene layers depend on the volume fraction of MXene and is given in Table 2 and the interface volume fraction is defined as function of the MXene volume fraction. The matrix volume fraction is calculated based on these two volume fraction values. These volume fractions are normalized for the purpose of generalization. Individual subroutine codes (in MATLAB code) are written for each analytical model and the results of stiffness matrix estimation is used to finally obtain effective Young's modulus values of the MXNC. The equations provided in Appendix A and B are implemented and Young's modulus is derived from the in-plane stiffness matrix for CLPT. The estimations of effective Young's modulus from the EIM and CLPT for MXene/Epoxy-resin nanocomposite are overestimation and underestimation, respectively, in comparison with the experimental (literature-based) and numerical results. For the MXene/PVA nanocomposite case both EIM and CLPT overestimate the effective Young's modulus. These estimation results from the analytical methods clearly indicate oversimplification of the models developed using these methods are less effective unless they can be modified and the underlying assumptions can be improved to capture more of the physics of the material being modeled.

The numerical model consists of RVE built with 8000 (20×20×20) polymeric matrix brick elements created in finite element method, but the number of MXene layers are chosen based on the volume fraction of MXenes defined by the configurations. The configurations given in Figure 2 and Table 2 are under consideration. The MXene monolayer modeled as plate elements have their nodal field variable linked to the nearest matrix brick element nodes using MPCs discussed in section 2.3.

Considering the results of numerical model results in Table 3 (b), in configuration 1, with increase of MXene weight fraction in epoxy-resin from 2.96 to 24.42 percent increased the effective Young's modulus by 7.5321 percent while for the configuration 2 we see a decrease in effective Young's modulus by 1.66 percent. The configuration 1 is a simple distribution of MXenes while the configuration 2 has edge overlap (interlock) nacre-mimetic brick-and-mortar assembly of MXenes. Configuration 3 models the nacre-mimetic brick-and-mortar assembly process with end interlock regions. Both configuration 2 & 3 can have controlled polymer interaction and has been demonstrated by experiments in literature [26]. In configuration 3, the increase in weight fraction of MXene in epoxy-resin from 1.093 to 5.0709 percent, 5.0709 to 14.9518 percent and 14.9518 to 42.12 percent results in the increase in effective Young's modulus of MXene/Epoxy-resin nanocomposites from 8.546 to 11.05705 and to 3.3659 percent, respectively. For an increase of MXene weight fraction from 1.093 to 14.9518 percent and 1.093 to 42.12 percent, the effective Young's modulus of configuration 3 increases by 21.1105 and 25.1817 percent, respectively. The strength (maximum stress capacity within elastic limits) of the RVEs are given in Table 3 (c). In configurations 1, 2 and 3, with the increase in MXene weight fraction in epoxy-resin from 2.96 to 24.42 percent, 5.67 to 42.12 percent and 1.093 to 42.12 percent, respectively, the strength increases by 1.7209, 42.374 and 11.9081 percent.

Along with the increase in MXene volume fraction, the assembly pattern of MXenes in the epoxy-resin also matters in improving the load bearing capacity and effective transfer of load from the polymer material to the MXene filler material. The bioinspired nacre-mimetic brick-and-mortar configurations used in configurations 2 & 3 indicate these enhanced physical behaviors of the MXene nanocomposite. Figure 5 (a-c) indicate these enhanced physical behaviors in which the polymer

Preprints (www.preprints.org) | NOT PEER-REVIEWED | Posted: 26 October 2020 doi:10.20944/preprints202010.0524.v1



experiences less stress, and the applied load is distributed among the MXenes according to the assembly pattern. Interestingly, the configuration 2 has the MXenes stacked along the direction of the quasi-static load and not sparsely distributed as in configuration 3, and we see a higher strength of the RVE (Figure 6 & Table 3 (b-c) provides illustrations of stress fields of the configurations). The sparsely distributed configuration 3 also has an increase in strength as well as increase in the effective Young's modulus. The interlocking mechanism between the MXene fillers brought in by the nacre-mimetic assembly allows for effective load transfer from polymer to MXenes and with increasing weight/volume fraction of MXenes, the strength and effective Young's modulus increases (configuration 3 shown in Figure 6 & Table 3 (b-c)). The nacre-mimetic brick-and-mortar assembly process offers advantage of tailoring the MXene assembly with polymer intercalation and this ensure a good load transfer as seen from the results in Table 3 (c). With controlled assembly of the MXenes with the polymer, along with the increase in the load bearing capacity, the damage propagation path might also be controlled as the crack propagation in such 2D nanocomposites are along the fillers [52].

**Table 2.** Implementation of the three configuration models using numerical method

| Volume Fraction of Filler vol% | Weight Fraction of filler wt. % | Number of MXene layers | Configuration 1 | Configuration 2 | Configuration 3 |
|---|---|---|---|---|---|
| 0.37844 | 1.093 | 17 | | | #### |
| 1 | 2.96 | 45 | **** | | |
| 1.8031 | 5.0709 | 81 | | | #### |
| 2 | 5.67 | 91 | | ++++ | |
| 5.6988 | 14.9518 | 256 | | | #### |
| 10 | 24.42 | 449 | **** | | |
| 20 | 42.12 | 899 | | ++++ | #### |

| | |
|---|---|
| Configuration 1 | **** |
| Configuration 2 | ++++ |
| Configuration 3 | #### |

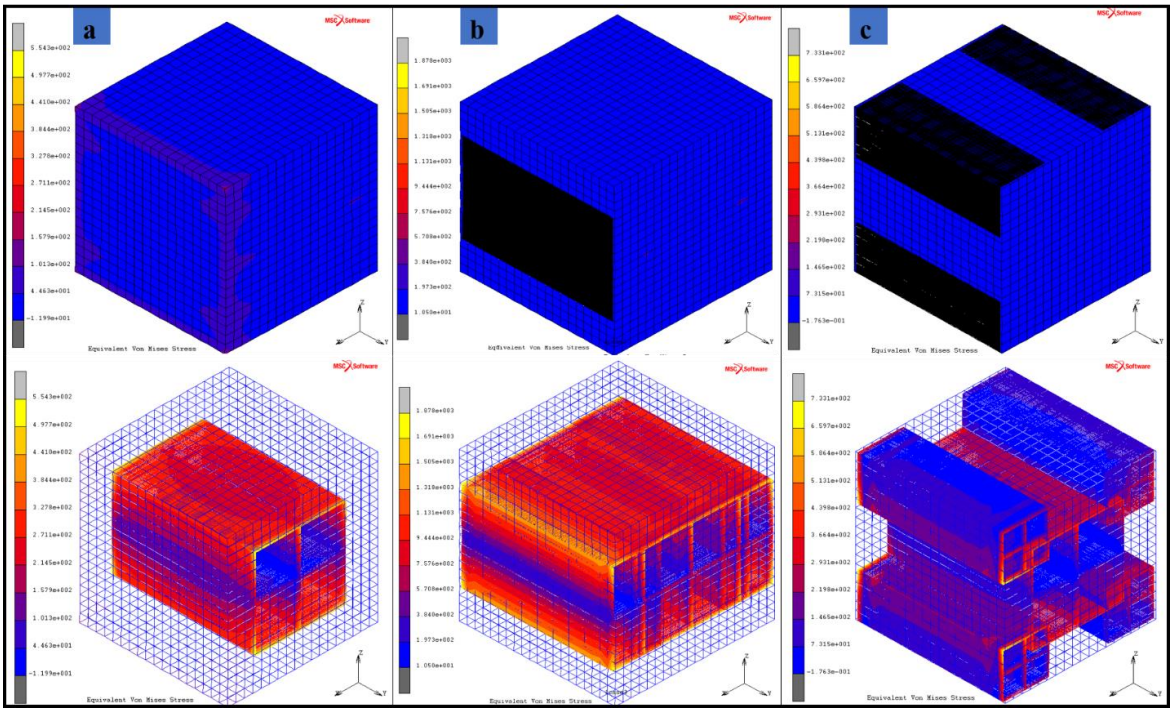

Preprints (www.preprints.org) | NOT PEER-REVIEWED | Posted: 26 October 2020 doi:10.20944/preprints202010.0524.v1



**Figure 5.** Stress field due to quasi-static tensile loading (X-direction) for various configurations (a) Configuration 1 – 24.42 wt. % of MXene in Epoxy-resin, (b) Configuration 2 – 42.12 wt. % of MXene in Epoxy, (c) Configuration 3 – 42.12 wt. % of MXene in Epoxy

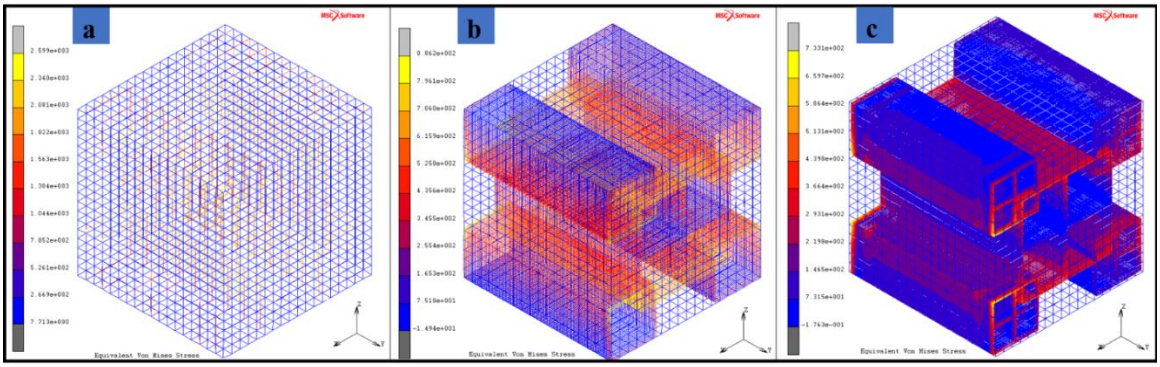


**Figure 6.** Stress field due to quasi-static tensile loading (X-direction) for Configuration 3 with varying weight fraction of MXene in Epoxy-resin. (a) 5.0709 wt. % of MXene in Epoxy, (b) 14.9518 wt. % of MXene in Epoxy, (c) 42.12 wt. % of MXene in Epoxy

*3.3. Comparisons with literature-based experimental results*

For MXene/Epoxy-resin nanocomposites shown in Table 3 (a & b), the EIM estimates the Young's modulus of the nanocomposite to be of an order of magnitude higher than reported experimental results if the weight fraction is above 10 wt.%, but the estimations for weight fraction below 10 wt.% of MXene is of the same order. The EIM results has overestimations compared to the reported experimental results [10]. The results from CLPT underestimate the effective nanocomposite Young's modulus by an order of magnitude as seen in Table 3 (a), except for weight fraction close to 40 wt.%. The interface Young's modulus employed in the EIM and CLPT methods has been shown in Table 3 (a).

The FEA results estimate the Young's modulus to be of same order as the reported experimental results. The FEA based results provide a more consistent estimation close to the reported experimental results for MXene/Epoxy-resin nanocomposite. Numerical results of configuration 3 shown in a black outline box in Table 3 (b) are compared with results presented in [11]. Error in estimation from numerical models in comparison with reported experimental results is in the range of 12.4 - 21.09 %. The quality of estimation of Young's modulus in relation to reported experimental results are shown in Figure 7. Numerical results show increase of Young's modulus value of MXNC with increase in weight fraction of MXene in composite. For the reported experimental result, there is an increase in the Young's modulus value, reaching a value of 4.37 GPa and then a reduction in the Young's modulus with respect to weight fraction of MXene in composite. The numerical model results provide a more consistent prediction compared to analytical models.

The same interface conditions presented in Table 3 are employed for the MXene/PVA nanocomposite results shown in Table 4. EIM, CLPT and modified CLPT reached the volume constraint condition (to restrict the fillers from modeled outside the RVE volume) imposed on the RVE models in the MATLAB code and hence the weight fraction values were at 38.06 % for EIM and CLPT and 38.09 % for modified CLPT method. The MXene/PVA nanocomposite numerical results are of the same order as those obtained experimentally in literature [8] but the reported experimental result value is more than twice that of the numerical one.

The various analytical and numerical models developed and tested against reported experimental results in this paper provide a wide range of possibilities for further model refinements. A designer based on the requirement can use the models in the process of pre-designing the MXNC. An estimation of nanocomposite properties from these models will allow the MXNC designer to select a model for composite properties simulation and compare it with models that are developed

Preprints (www.preprints.org) | NOT PEER-REVIEWED | Posted: 26 October 2020 doi:10.20944/preprints202010.0524.v1



in this paper. The advantages and drawbacks of these models concluded in this paper can support in design process.

**Table 3.** (a) MXene/Epoxy-resin nanocomposite analytical results

| MXene/Epoxy | Weight Fraction (wt %) | E experimental [11](GPa) | EIM (GPa) | CLPT (GPa) |
|---|---|---|---|---|
| Interface Layer E (GPa) | | | $1*10^{-3}$ | $3.25*10^{3}$ |
| | 1.093 | 3.62 | 3.998 | 0.1378 |
| | 2.96 | 4.1 | 5.7463 | 0.3517 |
| | 5.0709 | 4.37 | 7.74 | 0.5941 |
| | 5.67 | Not Available | 8.3274 | 0.6654 |
| | 14.9518 | 3.42 | 18.069 | 1.8419 |
| | 24.42 | Not Available | 29.578 | 3.2179 |
| | 39.52 | Not Available | 52.295 | 5.8916 |

**Table 3.** (b) MXene/Epoxy-resin nanocomposite numerical results compared with reported experimental results

| MXene/Epoxy | Weight Fraction (wt %) | E Numerical (GPa) | E experimental (GPa) [11] | Error in Estimation (%) |
|---|---|---|---|---|
| Configuration 1 (****) | 2.96 | 3.2554 | 4.1 | 20.60 |
| | 24.42 | 3.5006 | Not Available | Not Available |
| Configuration 2 (++++) | 5.67 | 3.4028 | Not Available | Not Available |
| | 42.12 | 3.346 | Not Available | Not Available |
| Configuration 3 (####) | 1.093 | 3.1769 | 3.62 | 12.24 |
| | 5.0709 | 3.4484 | 4.37 | 21.09 |
| | 14.9518 | 3.8474 | 3.42 | 12.50 |
| | 42.12 | 3.9769 | Not Available | Not Available |

**Table 3.** (c) MXene/Epoxy-resin nanocomposite numerical results compared with reported experimental results [11]

| MXene/Epoxy | Weight Fraction (wt %) | E Numerical (GPa) | Maximum Stress (MPa) | Maximum Strain |
|---|---|---|---|---|
| Configuration 1 (****) | 2.96 | 3.2554 | 63.92 | 0.0207 |
| | 24.42 | 3.5006 | 65.02 | 0.0204 |
| Configuration 2 (++++) | 5.67 | 3.4028 | 57.37 | 0.0189 |
| | 42.12 | 3.346 | 81.89 | 0.0258 |
| Configuration 3 (####) | 1.093 | 3.1769 | 63.99 | 0.0202 |
| | 5.0709 | 3.4484 | 65.97 | 0.0207 |
| | 14.9518 | 3.8474 | 66.56 | 0.0206 |
| | 42.12 | 3.9769 | 71.61 | 0.05716 |

Preprints (www.preprints.org) | NOT PEER-REVIEWED | Posted: 26 October 2020 doi:10.20944/preprints202010.0524.v1



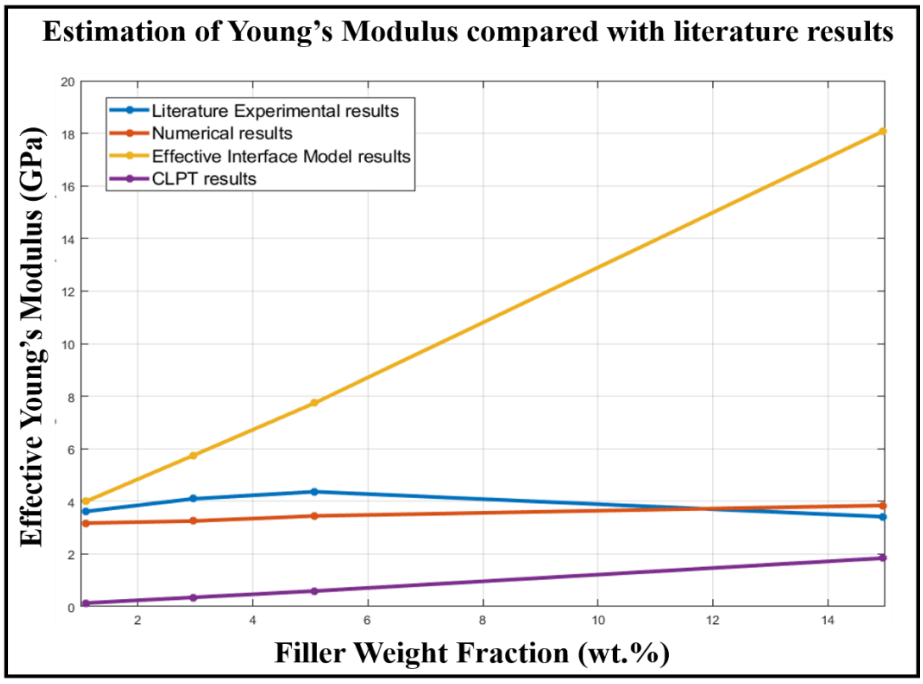


**Figure 6.** MXene/Epoxy-resin nanocomposite modeling results compare to reported experimental results

**Table 4.** MXene/PVA nanocomposite results

| MXene/PVA | E Numerical (GPa) | E experimental (GPa) [9] | EIM (GPa) | CLPT (GPa) |
|---|---|---|---|---|
| | [wt % = 42.12] | [wt % = 40] | [wt % = 38.06] | [wt % = 38.06] |
| Interface Layer EI (GPa) | Not considered | | $1*10^{-3}$ | $3.25*10^{3}$ |
| Configuration 2 (++++) | 1.4414 | 3.7 | 43.777 | 5.8876 |
| Configuration 3 (####) | 42.12 | | | |

*3.4. Discussions on influence of interface between MXenes and polymers*

The perfect bonding condition between MXene and polymer seems to be the cause of variation of estimation results in case of Epoxy-resin and PVA matrix-based nanocomposite. In both the cases, the surface termination of MXenes indicates to play a crucial role in bonding with the polymer chain in fabrication of MXNC and modeling it within the numerical models is an important step. The results also indicate that numerically obtained Young's modulus of MXene/PVA nanocomposite, is half in value to that of the experimental results obtained for PVA in literature. The increased strength of the composite compared with the pure PVA (approximate Young's modulus of 1 GPa), indicates a strong bonding between the hydroxyl group of PVA polymer chain and the surface termination of MXene. The effect of the size of MXene monolayers on the composite and interface bonding also needs further investigation. The surface termination of MXene can lead to two types of bonding as per the chemical bonding study [53]. Hydrogen and van-der-Waal type bonding are the two types of bonding that the surface termination might have with MXene or polymer. Both MD and experimental investigation of the effect of bonding can be adopted to the models presented in this paper. Several new MXenes [54] that are being discovered can be adopted to the models developed in this paper as well, particularly, the numerical models. Finally, the micromechanical models developed in this paper form a basis for multi-scale study of MXene mechanical properties in future. The models developed with numerical

 doi:10.20944/preprints202010.0524.v1



methods provide a consistent estimation of the Young's modulus of the nanocomposites compared to the analytical methods.

## 4. Conclusions

The paper focuses on developing models using bioinspired nacre-mimetic brick-and-mortar assembly of MXene with polymer matrix. Nacre-mimetic composites have had a history of providing good strength, toughness, damage resistance and effective load bearing capacity. These indications on nacre-mimetic assembly led to the development of MXene/Polymer nanocomposite configurations discussed in this paper. Experimental characterization of pure MXene samples were done to study the morphology and dimensionality of MXene samples and validate the observations made in the literature about MXene lateral dimensions and thickness. These MXenes with literature determined material properties were modeled with simple MXene distribution as in configuration 1 and with nacre-mimetic assembly with interlocking mechanism at the edges of the MXenes as in configuration 2 & 3. The models are analyzed using analytical models of EIM and CLPT with consideration of interface regions between MXene and polymer and numerical models using finite element method with MPC method considering perfect bonded condition between MXene and polymer.

On examination with classical analytical methods, the EIM overestimate the nanocomposite Young's modulus by an order of magnitude compared to reported experimental results up to 40 % weight fraction of MXene (up to 20 % volume fraction) in polymer. The CLPT method provides an estimation of the effective MXNC Young's modulus in the same order of magnitude or an order lesser than the reported experimental results. Further optimization and modifications of the CLPT method can refine the estimation. The numerical results provide the estimation of MXNC Young's modulus to be of the same order of magnitude as that of the reported experimental results and more consistent than the analytical methods. The estimation errors for the numerical models of MXene/Epoxy-resin nanocomposite compared to reported experimental results are less than 21 %. Results indicate that better models for bonding conditions between MXene/Epoxy-resin and MXene/PVA may lead to close quantitative estimations to reported experimental results.

Numerical methods using finite element method is applied to the three configurations including the bioinspired nacre-mimetic assembly in configuration 2 & 3 with varying MXene weight fraction. Effective Young's modulus and strength (maximum stress capacity within elastic limits) are estimated for the MXene/Polymer nanocomposite. Configurations 1, 2 and 3 with increase in MXene weight fraction in epoxy-resin of 2.9 to 24.4 percent, 5.6 to 42.1 percent and 1 to 42.1 percent, estimates an increase in effective Young's modulus by 7.5, 1.6 and 25.1 percent, respectively. The results provide an interesting insight that the nacre-mimetic brick-and-mortar assembly configuration of MXene with polymer intercalation can also play a role in controlling the elastic properties and help in control of effective load transfer from polymer material to MXene filler material. With the three configurations we observe that the nacre-mimetic configurations 2 and 3 which have interlocking mechanism assembly of MXenes with polymer have different load bearing capacity and the strength depends on the assembly pattern. The controlled assembly of MXene with polymer intercalation can result in better load bearing capacity of the nanocomposite by effective transfer of load to MXene filler and the damage propagation path can also be controlled with further optimization of the brick-and-mortar assembly process.

**Author Contributions:** Conceptualization, S.S., P.P., L.M., T.U. and K.G.; methodology, S.S., P.P., L.M. and K.G..; software, S.S.; validation, S.S..; formal analysis, S.S., P.P., L.M. and K.G.; investigation, S.S., P.P., L.M. and K.G.; resources, T.U.; writing—original draft preparation, S.S.; writing—review and editing, P.P., L.M. and K.G.; visualization, S.S.; supervision, T.U. and K.G.; project administration, T.U.; funding acquisition, T.U. All authors have read and agreed to the published version of the manuscript.

**Funding:** Authors at AGH UST have received funding for this project from the European Union's Horizon 2020 research and innovation programme (DyVirt - Dynamic Virtualization: modeling performance of engineering structures) under the Marie Skłodowska-Curie grant agreement No 764547.

**Acknowledgments:** The authors at AGH UST would like to acknowledge Material Research Centre, Ukraine, for the MXene samples supply and Dr. Katarzyna Berent and Dr. Marta Gajewska at AGH UST for their support in the experimental characterization of MXenes presented in the paper.

**Conflicts of Interest:** The authors declare no conflict of interest.

## Appendix A

Implementation of EIM: The implementation of EIM equations used in the paper are given here. Eqn. A1 provides the overall nanocomposite stiffness matrix C. Here the filler-matrix-filler interface and filler-matrix interface are assumed to have the same properties. The tensor $T_{fi}$ is the dilute strain concentration tensor of the filler considering the interface in the matrix and $T_f$ is the dilute strain concentration tensor of the filler alone and these are given in Eqn. A2 & A3. $V_i$, $V_f$ and $V_m$ are the volume fractions of the interface, filler, and matrix, respectively. This interface volume fraction has been made a function of the filler volume fraction considering the interface to be layers above and below each MXene monolayer as shown in Figure 2 & 4 in the paper. The interface is modeled using equivalent continuum approach there by providing the equations given below.

$$C = C_m + [(V_f + V_i)(C_i - C_m) + V_f(C_f - C_i)T_f][(V_m I + (V_f + V_i)T_{fi})]^{-1} \quad (A1)$$

$$T_f = I - S_f [S_f + C_m(C_f - C_m)^{-1}]^{-1} \quad (A2)$$

$$T_{fi} = I - S_f \left\{ \left( \frac{V_f}{V_i + V_f} \right) [S_f + C_m(C_f - C_m)^{-1}]^{-1} + \left( \frac{V_i}{V_i + V_f} \right) [S_f + C_m(C_i - C_m)^{-1}]^{-1} \right\} \quad (A3)$$

## Appendix B

Implementation of CLPT: The displacement and strain fields of the Kirchhoff's plate theory are given by Eqns. B1-B3 and Eqns. B4-B7, respectively. Displacements at any point on the plate are $u_1(x_1,x_2,x_3)$, $u_2(x_1,x_2,x_3)$ and $u_3(x_1,x_2,x_3)$, and displacements of the normal material line are $\bar{u}_1(x_1,x_2,x_3)$, $\bar{u}_2(x_1,x_2,x_3)$ and $\bar{u}_3(x_1,x_2,x_3)$, where $(x_1,x_2,x_3)$ are the positions along orthogonal unit basis vector ($b_1$, $b_2$, $b_3$) forming the user-defined coordinate axis. The rotations of the cross-section of the plate ($\varphi_1$, $\varphi_2$) are assumed to be derivatives of the out-of-plane (direction b3) displacement of the mid-plane of the plate. Based on these assumptions, displacement, strain and stress fields of the laminate can be computed as shown in [49,55]. The in-plane stiffness (A), bending stiffness(D) and coupled stiffness (B) matrices are calculated based on the Eqn. B8, B9 and B10. Because of the 2D plate structure assumption, the matrices reduce to a 3 × 3 matrix. The overall stiffness matrix (Q) is represented by the Eqn. B11. The constitutive relationship based on in-plane forces and deformation as well as bending moments and curvatures of the laminated stack can be represented by Eqn. B12. N and M are in-plane forces per unit length and bending moment per unit length while $\varepsilon_o$ and $\kappa$ are the mid-plane strains and curvature of the laminate stack. Eqn. B14 is the reduced stiffness matrix of each layer (can be of filler, matrix, or interface). The term with notation (.)ij indicates the layer number considering up to n layers (k = 1,2, 3,…,n). The in-plane stiffness matrix (A) depends on the thickness of each layer and this helps in considering any shape of the inclusion as discussed in section 3.2. The vectors and matrices are represented with bold letters as per the notation followed. The matrix S called the permutation matrix is introduced solely for the purpose of sign conventions.

$$u_1(x_1,x_2,x_3) = \overline{u_1}(x_1,x_2) - x_3\varphi_1;\ \varphi_1 = \left( \frac{\partial \overline{u_3}}{\partial x_1} \right) \quad (B1)$$

$$u_2(x_1,x_2,x_3) = \overline{u_2}(x_1,x_2) - x_3\varphi_2;\ \varphi_2 = \left( \frac{\partial \overline{u_3}}{\partial x_2} \right) \quad (B2)$$

$$u_3(x_1,x_2,x_3) = \overline{u_3}(x_1,x_2) \quad (B3)$$

Preprints (www.preprints.org) | NOT PEER-REVIEWED | Posted: 26 October 2020 doi:10.20944/preprints202010.0524.v1



$$\gamma_{13} = \gamma_{23} = 0 \tag{B4}$$

$$\epsilon_1 = \frac{\partial \overline{u_1}}{\partial x_1} - x_3 {\varphi_1}^2; {\varphi_1}^2 = \left(\frac{\partial^2 \overline{u_3}}{\partial x_1^2}\right) \tag{B5}$$

$$\epsilon_2 = \frac{\partial \overline{u_2}}{\partial x_2} - x_3 {\varphi_2}^2; {\varphi_2}^2 = \left(\frac{\partial^2 \overline{u_3}}{\partial x_2^2}\right) \tag{B6}$$

$$\gamma_{13} = \frac{\partial \overline{u_1}}{\partial x_2} + \frac{\partial \overline{u_2}}{\partial x_1} - 2x_3 \left(\frac{\partial^2 \overline{u_3}}{\partial x_1 \partial x_2}\right) \tag{B7}$$

$$\mathbf{A} = \begin{bmatrix} A_{11} & A_{12} & A_{13} \\ A_{21} & A_{22} & A_{23} \\ A_{31} & A_{32} & A_{33} \end{bmatrix} \tag{B8}$$

$$\mathbf{B} = \begin{bmatrix} B_{11} & B_{12} & B_{13} \\ B_{21} & B_{22} & B_{23} \\ B_{31} & B_{32} & B_{33} \end{bmatrix} \tag{B9}$$

$$\mathbf{D} = \begin{bmatrix} D_{11} & D_{12} & D_{13} \\ A_{21} & A_{22} & D_{23} \\ D_{31} & D_{32} & D_{33} \end{bmatrix} \tag{B10}$$

$$\mathbf{Q} = \left[\begin{array}{ccccc} A_{11} & A_{12} & A_{13}B_{11} & B_{12} & B_{13} \\ A_{21} & A_{22} & A_{23}B_{21} & B_{22} & B_{23} \\ A_{31} & A_{32} & A_{33}B_{31} & B_{32} & B_{33} \\ \hline B_{11} & B_{12} & B_{13}D_{11} & D_{12} & D_{13} \\ B_{21} & B_{22} & B_{23}A_{21} & A_{22} & D_{23} \\ B_{31} & B_{32} & B_{33}D_{31} & D_{32} & D_{33} \end{array}\right] \tag{B11}$$

$$\begin{Bmatrix} \mathbf{N} \\ \mathbf{SM} \end{Bmatrix} = \begin{bmatrix} \mathbf{A} & \mathbf{B} \\ \mathbf{B} & \mathbf{D} \end{bmatrix} \begin{Bmatrix} \boldsymbol{\varepsilon_o} \\ \mathbf{S}\boldsymbol{\kappa} \end{Bmatrix} \tag{B12}$$

$$\mathbf{S} = \begin{bmatrix} 0 & 1 & 0 \\ -1 & 0 & 0 \\ 0 & 0 & -1 \end{bmatrix} \tag{B13}$$

$$\mathbf{C} = \begin{bmatrix} C_{11} & C_{12} & C_{16} \\ C_{21} & C_{22} & C_{26} \\ C_{61} & C_{62} & C_{66} \end{bmatrix} \tag{B14}$$

## Appendix C

Element 75 and 7 of MSC Marc: Eqn. D1-D5 (h is the single plate thickness) provides the strain expressions equations used to model the thick-plate elements of MXenes in numerical analysis. The displacement field are same as Eqn. C1-C3.

$$\epsilon_1 = \frac{\partial \overline{u_1}}{\partial x_1} + x_3 \widehat{\varphi_2};\ \widehat{\varphi_2} = \left(\frac{\partial \varphi_2}{\partial x_1}\right) \tag{C1}$$

$$\epsilon_2 = \frac{\partial \overline{u_2}}{\partial x_2} - x_3 \widehat{\varphi_1};\ \widehat{\varphi_1} = \left(\frac{\partial \varphi_1}{\partial x_2}\right) \tag{C2}$$

$$\epsilon_{12} = \frac{1}{2}\left[\left(\frac{\partial \overline{u_1}}{\partial x_2} + \frac{\partial \overline{u_2}}{\partial x_1}\right) + x_3 \left(\frac{\partial \varphi_2}{\partial x_2} - \frac{\partial \varphi_1}{\partial x_1}\right)\right] \tag{C3}$$

$$\epsilon_{23} = \left(\frac{\partial \overline{u_3}}{\partial x_2} - \varphi_1\right)\left(1 - \frac{4}{h^2} {x_3}^2\right) \tag{C4}$$

$$\epsilon_{23} = \left(\frac{\partial \overline{u_3}}{\partial x_1} - \varphi_2\right)\left(1 - \frac{4}{h^2}{x_3}^2\right) \quad \text{(C5)}$$

The displacement assumption and mapping from x-y-z space or b1-b2-b3 space into a cube in the ξ, η, ζ space is give below. Eqn. D6 & D7 are the coordinate transformation equations used in MSC Marc and provided by developer [46].

$$x = a_0 + a_1\xi + a_2\eta + a_3\zeta + a_4\xi\eta + a_5\zeta\xi + a_6\xi\zeta + a_7\zeta\xi\eta \quad \text{(C6)}$$

$$\psi = b_0 + b_1\xi + b_2\eta + b_3\zeta + b_4\xi\eta + b_5\zeta\xi + b_6\xi\zeta + b_7\zeta\xi\eta \quad \text{(C7)}$$

Function or coordinate expressed through nodal quantities using integration function are given below. Eqn. C8 provides the elemental to global displacement transformation and Eqn. C9 – C16 are the shape functions used in the process of the transformation.

$$x = \sum_{i=1}^{8} x_i\rho_i \quad \text{(C8)}$$

$$\rho_1 = \frac{1}{8}(1-\xi)(1-\eta)(1-\zeta) \quad \text{(C9)}$$

$$\rho_2 = \frac{1}{8}(1+\xi)(1-\eta)(1-\zeta) \quad \text{(C10)}$$

$$\rho_3 = \frac{1}{8}(1+\xi)(1+\eta)(1-\zeta) \quad \text{(C11)}$$

$$\rho_4 = \frac{1}{8}(1-\xi)(1+\eta)(1-\zeta) \quad \text{(C12)}$$

$$\rho_5 = \frac{1}{8}(1-\xi)(1-\eta)(1+\zeta) \quad \text{(C13)}$$

$$\rho_6 = \frac{1}{8}(1+\xi)(1-\eta)(1+\zeta) \quad \text{(C14)}$$

$$\rho_7 = \frac{1}{8}(1+\xi)(1+\eta)(1+\zeta) \quad \text{(C15)}$$

$$\rho_8 = \frac{1}{8}(1-\xi)(1+\eta)(1+\zeta) \quad \text{(C16)}$$

## References


1. Han, Y.; Ge, Y.; Chao, Y.; Wang, C.; Wallace, G.G. Recent progress in 2D materials for flexible supercapacitors. *J. Energy Chem.* **2018**, *27*, 57–72, doi:10.1016/j.jechem.2017.10.033.
2. Sadeghi, F.; Sarvi, A.; Sundararaj, U. PVDF / Carbonnanotubes / Nanoclay Composites for Piezoelectric Applications. **2014**, 81–87.
3. Cullinan, M.A.; Culpepper, M.L. Carbon nanotubes as piezoresistive microelectromechanical sensors: Theory and experiment. *Phys. Rev. B - Condens. Matter Mater. Phys.* **2010**, *82*, 1–6, doi:10.1103/PhysRevB.82.115428.
4. Sarycheva, A.; Polemi, A.; Liu, Y.; Dandekar, K.; Anasori, B.; Gogotsi, Y. 2D titanium carbide (MXene) for wireless communication. *Sci. Adv.* **2018**, *4*, 1–9, doi:10.1126/sciadv.aau0920.
5. Chinke, S.L.; Sandhu, I.S.; Saroha, D.R.; Alegaonkar, P.S. Graphene-Like Nanoflakes for Shock Absorption Applications. *ACS Appl. Nano Mater.* **2018**, *1*, 6027–6037, doi:10.1021/acsanm.8b01061.
6. Wang, G.; Dai, Z.; Xiao, J.; Feng, S.Z.; Weng, C.; Liu, L.; Xu, Z.; Huang, R.; Zhang, Z. Bending of Multilayer van der Waals Materials. *Phys. Rev. Lett.* **2019**, *123*, 116101, doi:10.1103/PhysRevLett.123.116101.

7. Tian, W.; VahidMohammadi, A.; Reid, M.S.; Wang, Z.; Ouyang, L.; Erlandsson, J.; Pettersson, T.; Wågberg, L.; Beidaghi, M.; Hamedi, M.M. Multifunctional Nanocomposites with High Strength and Capacitance Using 2D MXene and 1D Nanocellulose. *Adv. Mater.* **2019**, *1902977*, 1902977, doi:10.1002/adma.201902977.
8. Naguib, M.; Kurtoglu, M.; Presser, V.; Lu, J.; Niu, J.; Heon, M.; Hultman, L.; Gogotsi, Y.; Barsoum, M.W. Two-Dimensional Nanocrystals Produced by Exfoliation of Ti3AlC2. *Adv. Mater.* **2011**, *23*, 4248–4253, doi:10.1002/adma.201102306.
9. Ling, Z.; Ren, C.E.; Zhao, M.-Q.; Yang, J.; Giammarco, J.M.; Qiu, J.; Barsoum, M.W.; Gogotsi, Y. Flexible and conductive MXene films and nanocomposites with high capacitance. *Proc. Natl. Acad. Sci.* **2014**, *111*, 16676–16681, doi:10.1073/pnas.1414215111.
10. Lipatov, A.; Lu, H.; Alhabeb, M.; Anasori, B.; Gruverman, A.; Gogotsi, Y.; Sinitskii, A. Elastic properties of 2D Ti 3 C 2 T x MXene monolayers and bilayers. *Sci. Adv.* **2018**, *4*, eaat0491, doi:10.1126/sciadv.aat0491.
11. Wang, L.; Chen, L.; Song, P.; Liang, C.; Lu, Y.; Qiu, H.; Zhang, Y.; Kong, J. Fabrication on the annealed Ti 3 C 2 T x MXene / Epoxy nanocomposites for electromagnetic interference shielding application. *Compos. Part B* **2019**, *171*, 111–118, doi:10.1016/j.compositesb.2019.04.050.
12. Srivatsa, S.; Belthangadi, P.; Ekambaram, S.; Pai, M.; Sen, P.; Uhl, T.; Kumar, S.; Grabowski, K.; Nayak, M.M. Dynamic response study of Ti3C2-MXene films to shockwave and impact forces. *RSC Adv.* **2020**, *10*, 29147–29155, doi:10.1039/D0RA04879H.
13. Habib, T.; Zhao, X.; Shah, S.A.; Chen, Y.; Sun, W.; An, H.; Lutkenhaus, J.L.; Radovic, M.; Green, M.J. Oxidation stability of Ti3C2Tx MXene nanosheets in solvents and composite films. *npj 2D Mater. Appl.* **2019**, *3*, 8, doi:10.1038/s41699-019-0089-3.
14. Weng, G.M.; Li, J.; Alhabeb, M.; Karpovich, C.; Wang, H.; Lipton, J.; Maleski, K.; Kong, J.; Shaulsky, E.; Elimelech, M.; et al. Layer-by-Layer Assembly of Cross-Functional Semi-transparent MXene-Carbon Nanotubes Composite Films for Next-Generation Electromagnetic Interference Shielding. *Adv. Funct. Mater.* **2018**, *28*, doi:10.1002/adfm.201803360.
15. Lipton, J.; Weng, G.-M.; Alhabeb, M.; Maleski, K.; Antonio, F.; Kong, J.; Gogotsi, Y.; Taylor, A. Mechanically Strong and Electrically Conductive Multilayer MXene Nanocomposites. *Nanoscale* **2019**, 1–18, doi:10.1039/c9nr06015d.
16. Lipton, J.; Weng, G.M.; Röhr, J.A.; Wang, H.; Taylor, A.D. Layer-by-Layer Assembly of Two-Dimensional Materials: Meticulous Control on the Nanoscale. *Matter* **2020**, *2*, 1148–1165, doi:10.1016/j.matt.2020.03.012.
17. Runesson, K.; Larsson, F. Computational Homogenization and Multiscale Modeling. **2011**.
18. Pan, Y.; Iorga, L.; Pelegri, A.A. Numerical generation of a random chopped fiber composite RVE and its elastic properties. *Compos. Sci. Technol.* **2008**, *68*, 2792–2798, doi:10.1016/j.compscitech.2008.06.007.
19. Wang, C.; Lyu, D. Multiscale cohesive zone modeling and simulation of high-speed impact, penetration, and fragmentation. *J. Micromechanics Mol. Phys.* **2018**, *03*, 1850003, doi:10.1142/s2424913018500030.
20. Kochmann, D.M.; Hopkins, J.B.; Valdevit, L. Multiscale modeling and optimization of the mechanics of hierarchical metamaterials. *MRS Bull.* **2019**, *44*, 773–781, doi:10.1557/mrs.2019.228.
21. Borysiuk, V.N.; Mochalin, V.N.; Gogotsi, Y. Molecular dynamic study of the mechanical properties of two-dimensional titanium carbides Tin+1Cn(MXenes). *Nanotechnology* **2015**, *26*, 1–10, doi:10.1088/0957-4484/26/26/265705.
22. Borysiuk, V.N.; Mochalin, V.N.; Gogotsi, Y. Bending rigidity of two-dimensional titanium carbide (MXene) nanoribbons: A molecular dynamics study. *Comput. Mater. Sci.* **2018**, *143*, 418–424,

doi:10.1016/j.commatsci.2017.11.028.

23. Monastyreckis, G.; Jr, L.M.; Hatter, C.B.; Aniskevich, A.; Gogotsi, Y.; Zeleniakiene, D. Micromechanical modeling of MXene-polymer composites. *Carbon N. Y.* **2020**, *162*, 402–409, doi:10.1016/j.carbon.2020.02.070.
24. Srivatsa, S.; Kumar, S.; Grabowski, K.; Jain, P.; Nayak, M.M.; Uhl, T.; Sen, P. Numerical and experimental investigations of pure MXene (Ti3C2Tx) film and MXene nanocomposites for structural health monitoring (Conference Presentation).; 2020; p. 99.
25. Qi, H.J.; Bruet, B.J.F.; Palmer, J.S.; Ortiz, C.; Boyce, M.C. Micromechanics and Macromechanics of the Tensile Deformation of Nacre. In *Mechanics of Biological Tissue*; Holzapfel, G.A., Ogden, R.W., Eds.; Springer Berlin Heidelberg: Berlin, Heidelberg, 2006; pp. 189–203 ISBN 978-3-540-31184-3.
26. Lipton, J.; Weng, G.-M.; Alhabeb, M.; Maleski, K.; Antonio, F.; Kong, J.; Gogotsi, Y.; Taylor, A.D. Mechanically strong and electrically conductive multilayer MXene nanocomposites. *Nanoscale* **2019**, *11*, 20295–20300, doi:10.1039/C9NR06015D.
27. Shi, X.; Wang, H.; Xie, X.; Xue, Q.; Zhang, J.; Kang, S.; Wang, C.; Liang, J.; Chen, Y. Bioinspired Ultrasensitive and Stretchable MXene-Based Strain Sensor via Nacre-Mimetic Microscale "brick-and-Mortar" Architecture. *ACS Nano* **2019**, *13*, 649–659, doi:10.1021/acsnano.8b07805.
28. Katti, K.S.; Katti, D.R.; Pradhan, S.M.; Bhosle, A. Platelet interlocks are the key to toughness and strength in nacre. *J. Mater. Res.* **2005**, *20*, 1097–1100, doi:10.1557/JMR.2005.0171.
29. Mishnaevsky, L.; Tsapatsis, M. Hierarchical materials: Background and perspectives. *MRS Bull.* **2016**, *41*, 661–664, doi:10.1557/mrs.2016.189.
30. Luz, G.M.; Mano, J.F. Biomimetic Design of Materials and Biomaterials Inspired by the Structure of Nacre. *Philos. Trans. Math. Phys. Eng. Sci.* **2009**, *367*, 1587–1605.
31. Mishnaevsky, L. Mesoscale Level in the Mechanics of Materials. In *Computational Mesomechanics of Composites*; John Wiley & Sons, Ltd: Chichester, UK, 2007; pp. 13–36 ISBN 9780470513170.
32. Mishnaevsky, L. *Computational Mesomechanics of Composites*; John Wiley & Sons, Ltd: Chichester, UK, 2008; ISBN 9780470513170.
33. Smith, B.L.; Schäffer, T.E.; Vlani, M.; Thompson, J.B.; Frederick, N.A.; Klndt, J.; Belcher, A.; Stucky, G.D.; Morse, D.E.; Hansma, P.K. Molecular mechanistic origin of the toughness of natural adhesives, fibres and composites. *Nature* **1999**, *399*, 761–763, doi:10.1038/21607.
34. Shahzad, F.; Alhabeb, M.; Hatter, C.B.; Anasori, B.; Man Hong, S.; Koo, C.M.; Gogotsi, Y. Electromagnetic interference shielding with 2D transition metal carbides (MXenes). *Science (80-. ).* **2016**, *353*, 1137–1140, doi:10.1126/science.aag2421.
35. Odegard, G.M.; Clancy, T.C.; Gates, T.S. Modeling of the Mechanical Properties of Nanoparticle / Polymer Composites. **2005**, *46*, 553–562.
36. Love, A.E.H. On the small free vibrations and deformations of elastic shells. *Philos. trans* **1888**, *s?rie*, 491?549.
37. Maleski, K.; Ren, C.E.; Zhao, M.Q.; Anasori, B.; Gogotsi, Y. Size-Dependent Physical and Electrochemical Properties of Two-Dimensional MXene Flakes. *ACS Appl. Mater. Interfaces* **2018**, *10*, 24491–24498, doi:10.1021/acsami.8b04662.
38. Fu, Z.H.; Zhang, Q.F.; Legut, D.; Si, C.; Germann, T.C.; Lookman, T.; Du, S.Y.; Francisco, J.S.; Zhang, R.F. Stabilization and strengthening effects of functional groups in two-dimensional titanium carbide. **2016**, *104103*, 1–10, doi:10.1103/PhysRevB.94.104103.
39. Kurtoglu, M.; Naguib, M.; Gogotsi, Y.; Barsoum, M.W. First principles study of two-dimensional early

transition metal carbides. *MRS Commun.* **2012**, *2*, 133–137, doi:10.1557/mrc.2012.25.

40. Lipatov, A.; Alhabeb, M.; Lukatskaya, M.R.; Boson, A.; Gogotsi, Y.; Sinitskii, A. Effect of Synthesis on Quality, Electronic Properties and Environmental Stability of Individual Monolayer Ti 3 C 2 MXene Flakes. *Adv. Electron. Mater.* **2016**, *2*, 1600255, doi:10.1002/aelm.201600255.
41. Mark, J.E. Polymer Data Handbook, 2nd ed. *J. Am. Chem. Soc.* **2009**, *131*, 16330, doi:10.1021/ja907879q.
42. Eshelby, J.D. The Determination of the Elastic Field of an Ellipsoidal Inclusion, and Related Problems. *Proc. R. Soc. A Math. Phys. Eng. Sci.* **1957**, *241*, 376–396, doi:10.1098/rspa.1957.0133.
43. Duan, H.L.; Wang, J.; Karihaloo, B.L. Theory of Elasticity at the Nanoscale. *Adv. Appl. Mech.* **2009**, *42*, 1–68, doi:10.1016/S0065-2156(08)00001-X.
44. Weinberger, C.; Cai, W.; Barnett, D. Stanford University ME340B Lecture Notes – Elasticity of Microscopic Structures Available online: http://micro.stanford.edu/~caiwei/me340b/content/me340b-notes_v01.pdf.
45. Kouznetsova, V.; Brekelmans, W.A.M.; Baaijens, F.P.T. An approach to micro-macro modeling of heterogeneous materials. **2001**, *27*.
46. Krzysztof Grabowski Design and Development of the Sensors for Structural Health Monitoring ( SHM ) based on the Carbon Nanomaterials, AGH University of Science and Technology, 2017.
47. Software, M. *Marc 2013 Volume B: Element Library*; 2013th ed.;
48. Tanov, R.; Tabiei, A. A Simple Correction to the First Order Shear Deformation Shell Finite Element Formulations Available online: https://www.dynalook.com/conferences/international-conf-2000/session8-1.pdf.
49. Chopra, I.; Sirohi, J. *Smart Structures Theory*; Cambridge Aerospace Series; Cambridge University Press: Cambridge, 2013; ISBN 9781139025164.
50. Kochmann, D.M. Computational Multiscale Modeling. **2018**.
51. Li, X.; Liu, Q.; Zhang, J. A micro-macro homogenization approach for discrete particle assembly - Cosserat continuum modeling of granular materials. *Int. J. Solids Struct.* **2010**, *47*, 291–303, doi:10.1016/j.ijsolstr.2009.09.033.
52. Dai, G.; Mishnaevsky, L. Graphene reinforced nanocomposites: 3D simulation of damage and fracture. *Comput. Mater. Sci.* **2014**, *95*, 684–692, doi:10.1016/j.commatsci.2014.08.011.
53. Liu, Y.; Zhu, X.; Pan, L. Hybrid Architectures based on 2D MXenes and Low-Dimensional Inorganic Nanostructures : Methods , Synergies , and Energy-Related Applications. **2018**, *1803632*, 1–22, doi:10.1002/smll.201803632.
54. Lipatov, A.; Alhabeb, M.; Lu, H.; Zhao, S.; Loes, M.J.; Vorobeva, N.S.; Dall'Agnese, Y.; Gao, Y.; Gruverman, A.; Gogotsi, Y.; et al. Electrical and Elastic Properties of Individual Single-Layer Nb 4 C 3 T x MXene Flakes. *Adv. Electron. Mater.* **2020**, *1901382*, 1901382, doi:10.1002/aelm.201901382.
55. Bauchau, O.A.; Craig, J.I. *Structural Analysis with Application to Aerospace Structures*; Bauchau, O.A., Craig, J.I., Eds.; Solid Mechanics and Its Applications; 1st ed.; Springer Netherlands: Dordrecht, 2009; Vol. 163; ISBN 978-90-481-2515-9.